

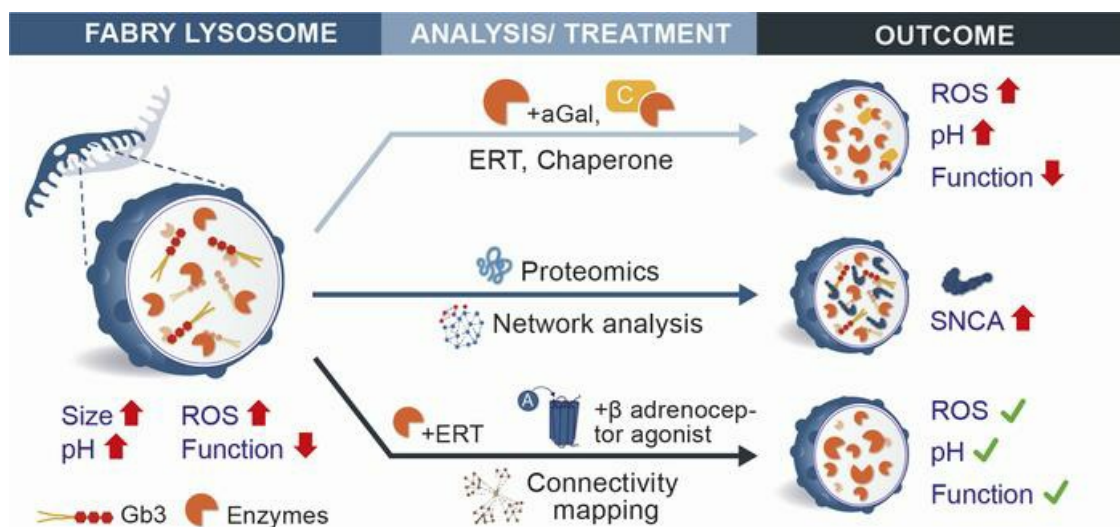
Synuclein α accumulation mediates podocyte injury in Fabry nephropathy

Fabian Braun, ... , Christoph Schell, Tobias B. Huber

J Clin Invest. 2023. <https://doi.org/10.1172/JCI157782>.

Research In-Press Preview Genetics Nephrology

Graphical abstract



Find the latest version:

<https://jci.me/157782/pdf>



Synuclein alpha accumulation mediates podocyte injury in Fabry nephropathy

Authors:

Fabian Braun^{1,2*}, Ahmed Abed^{3*}, Dominik Sellung^{3§}, Manuel Rogg^{3,4}, Mathias Woidy^{5,6}, Oysten Eikrem^{7,8}, Nicola Wanner^{1,2}, Jessica Gambardella^{9,10}, Sandra D Laufer^{1,2}, Fabian Haas^{1,2}, Milagros N Wong^{1,2,11,12}, Bernhard Dumoulin^{1,2}, Paula Rischke^{1,2}, Anne Mühlig^{1,2,5,6}, Wiebke Sachs^{2,13}, Katharina von Cossel¹⁴, Kristina Schulz^{1,2}, Nicole Muschol¹⁴, Sören W Gersting^{5,6}, Ania C Muntau⁵, Oliver Kretz^{1,2}, Oliver Hahn^{15,16}, Markus M Rinschen^{1,2,15,16}, Michael Mauer¹⁷, Tillmann Bork³, Florian Grahammer^{1,2}, Wei Liang³, Thorsten Eierhoff^{18,19}, Winfried Römer^{18,20}, Arne Hansen^{21,22}, Catherine Meyer-Schwesinger^{2,13}, Guido Iaccarino^{9,10}, Camilla Tøndel^{7,23}, Hans-Peter Marti^{7,8}, Behzad Najafian²⁴, Victor G Puelles^{1,2,11,12#}, Christoph Schell^{3,4,20#} and Tobias B Huber^{1,2#}

Affiliations:

- ¹III. Department of Medicine, University Medical Center Hamburg-Eppendorf, Hamburg, Germany
²Hamburg Center for Kidney Health (HCKH), University Medical Center Hamburg-Eppendorf, Hamburg, Germany
³Department of Medicine IV, Medical Center – University of Freiburg, Faculty of Medicine, University of Freiburg, Germany
⁴Institute of Surgical Pathology, Medical Center – University of Freiburg, Faculty of Medicine, University of Freiburg, Germany
⁵University Children's Hospital, University Medical Center Hamburg-Eppendorf, Hamburg, Germany
⁶University Children's Research, University Medical Center Hamburg-Eppendorf, Hamburg, Germany
⁷Department of Clinical Medicine, University of Bergen, Norway
⁸Department of Medicine, Haukeland University Hospital, Bergen, Norway
⁹Department of Advanced Biomedical Sciences, Federico II University, Napoli, Italy
¹⁰Interdepartmental Center of Research on Hypertension and Related Conditions, Federico II University, Napoli, Italy
¹¹Department of Clinical Medicine, Aarhus University, Aarhus, Denmark
¹²Department of Pathology, Aarhus University Hospital, Aarhus, Denmark
¹³Institute of Cellular and Integrative Physiology, Center for Experimental Medicine, University Medical Center Hamburg-Eppendorf, Hamburg, Germany
¹⁴Department of Pediatrics, International Center for Lysosomal Disorders (ICLD), University Medical Center Hamburg-Eppendorf, Hamburg, Germany
¹⁵Department of Biomedicine, Aarhus University, 8000 Aarhus, Denmark.
¹⁶Aarhus Institute for Advanced Studies, Aarhus University, 8000 Aarhus, Denmark.
¹⁷Departments of Pediatrics and Medicine, University of Minnesota, Minneapolis, MN, USA
¹⁸Faculty of Biology and Signalling Research Centres BIOS and CIBS, Albert-Ludwigs-University Freiburg, Freiburg, Germany
¹⁹Department of Vascular and Endovascular Surgery, University Hospital of Münster, Münster, Germany.
²⁰Freiburg Institute for Advanced Studies (FRIAS), University of Freiburg, Freiburg, Germany
²¹University Medical Center Hamburg-Eppendorf, Department of Experimental Pharmacology and Toxicology, 20246 Hamburg, Germany
²²German Center for Heart Research (DZHK), Partner site Hamburg/Lübeck/Kiel, Germany
²³Department of Pediatrics, Haukeland University Hospital, Bergen, Norway
²⁴Department of Laboratory Medicine & Pathology, University of Washington, Seattle, WA, USA

[§]Current address of DS: Department of Neurology, Heimer Institute for Muscle Research, University Hospital Bergmannsheil, Ruhr-University Bochum, Bochum, Germany.

Equal contributions as co-first (*) and as co-senior/corresponding (#) authors

Corresponding authors:

Tobias B. Huber

III. Department of Medicine, University Medical Center Hamburg-Eppendorf
t.huber@uke.de

Christoph Schell

Institute of Surgical Pathology, University Medical Center Freiburg
christoph.schell@uniklinik-freiburg.de

Victor G. Puelles

III. Department of Medicine, University Medical Center Hamburg-Eppendorf, and
Department of Clinical Medicine, Aarhus University
v.puelles@uke.de or vgpuelles@clin.au.dk

Abstract

Current therapies for Fabry disease are based on reversing intracellular accumulation of globotriaosylceramide (Gb3) by enzyme replacement therapy (ERT) or chaperone-mediated stabilization of the defective enzyme, thereby alleviating lysosomal dysfunction. However, their effect in the reversal of end-organ damage, like kidney injury and chronic kidney disease remains unclear. In this study, ultrastructural analysis of serial human kidney biopsies showed that long-term use of ERT reduced Gb3 accumulation in podocytes but did not reverse podocyte injury. Then, a CRISPR/CAS9-mediated α -Galactosidase knockout podocyte cell line confirmed ERT-mediated reversal of Gb3 accumulation without resolution of lysosomal dysfunction. Transcriptome-based connectivity mapping and SILAC-based quantitative proteomics identified alpha-synuclein (SNCA) accumulation as a key event mediating podocyte injury. Genetic and pharmacological inhibition of SNCA improved lysosomal structure and function in Fabry podocytes, exceeding the benefits of ERT. Together, this work reconceptualizes Fabry-associated cell injury beyond Gb3 accumulation, and introduces SNCA modulation as a potential intervention, especially for patients with Fabry nephropathy.

Introduction

Anderson-Fabry disease (FD) is an X-linked lysosomal storage disorder caused by mutations in the *GLA* gene (1), which results in an impairment of the hydrolase alpha-Galactosidase A (aGAL). This enzyme deficiency leads to lysosomal dysfunction (2) via progressive accumulation of globotriaosylceramide (Gb3) and other glycosphingolipids (3) in most cells of the body (4). Patients with FD suffer from extensive and progressive end-organ damage, for example cardiomyopathy and nephropathy, both of which being key factors for long-term survival (5).

The first therapies became available in 2001 with enzyme replacement therapy (ERT) (6, 7) and were complemented by chaperone therapy in 2016 (8). All have proven efficient in decreasing Gb3 deposits (9–14), but their impact on the reversal of end-organ damage remains unclear.

Glomerular epithelial cells (podocytes) are primary targets in chronic kidney diseases that progress to the requirement of dialysis or transplantation (15–18). Since podocytes exhibit limited regenerative capacities (19, 20), injury and loss are considered critical steps in renal pathophysiology and central therapeutic targets. Previous studies have shown podocytes to accumulate the highest amount of Gb3 in Fabry nephropathy, resulting in early (micro-)albuminuria (21, 22). However, the molecular mechanisms of Fabry podocytopathy remain elusive, in part due to limited access to human biopsy material. Furthermore, existing animal models do not completely reflect the human phenotype, especially those observed in Fabry nephropathy (23–25).

In this study, we report prevailing signs of podocyte damage in human kidney biopsies before and after ERT despite significant Gb3 reduction. We established a CRISPR/Cas9-based *GLA* knockout in human podocytes, which recapitulates classical cell injury features like lysosomal dysfunction. Quantitative proteomics combined with a network medicine approach identified the accumulation of alpha-Synuclein (SNCA) as a mediator of lysosomal dysfunction resistant to ERT both in vitro and in patient biopsies. This is the first report showing that accumulation of SNCA directly contributes to lysosomal impairment and disease severity in FD in a substrate independent fashion, which suggests that pharmacological targeting of SNCA could serve as an additional therapeutic strategy, especially for patients with Fabry nephropathy.

Results

Podocyte injury persists despite of ERT and significant reductions in Gb3 deposits

Ultrastructural analysis of serial human kidney biopsies (full demographics available in **Table S1**) revealed typical accumulation of Gb3 within podocytes combined with classical signs of podocyte injury, including alterations in foot process morphology (**Fig. 1A**). Enzyme replacement therapy partially reversed this phenotype by reducing podocyte-specific Gb3 inclusions. Importantly, increased foot process width remained unaffected (**Fig. 1B**), highlighting the possibility of alternative pathomechanisms in Fabry podocytopathy.

*Generation of a *GLA*-deficient podocyte line using CRISPR/Cas9 genome editing*

Next, we developed a novel in vitro system to model FD-related podocyte damage. Using two independent guide-RNAs (gRNAs), the first exon within the *GLA* locus was targeted to generate *GLA*-deficient immortalized male human podocytes (26)

using CRISPR/Cas9 (27, 28) (**Fig. 1C**) (29, 30). Subclones with mutations resulting in premature STOP codons (**Fig. S1A**) and efficient knockout on the protein level (**Fig. 1C**) were selected for further analyses. aGAL protein levels and activity were almost completely abolished (**Fig. 1D-E**), resulting in a significant increase of Gb3 in both thin layer chromatography (**Fig. S1B**) and lipid mass spectrometry (**Fig. 1F** and **Fig. S1C-E**) that decreased to baseline after treatment with recombinant aGAL. Multilaminar inclusions (zebra bodies) were detected within *GLA*-deficient podocytes with almost complete clearance of these structures after aGAL treatment (**Fig. 1G**).

In vitro ERT does not fully revert podocyte injury

Both lysosomal number as well as size were dramatically increased in *GLA* knockout clones and were partially reversed by aGAL treatment (**Fig. 1H** and **Fig. 1I**). These structural abnormalities were associated with impairment of lysosomal function. Recombinant aGAL treatment did not modify lysosomal pH or oxidative stress via reactive oxygen species (ROS). As the latter could be a result of mitochondrial dysfunction, we investigated oxygen consumption rate (OCR) and (**Fig. 1J**) mitochondrial morphology (**Fig. 1K**) and detected no differences between wildtype and knockout clones.

Podocytes are known for their prominent autophagy features (29) and we detected an increase in autophagy via the decrease of surrogate marker p62, while LC3-II was unchanged both at baseline and in chloroquine challenged KO cells (**Fig. S2**). Together, our data suggests that podocyte injury extends beyond substrate accumulation, as multiple features of FD are only ameliorated by aGAL replacement.

*SNCA accumulates in *GLA*-deficient podocytes and is resistant to short-term ERT*

We employed SILAC-based quantitative proteomics and transcriptome profiling via RNA sequencing to determine potential alterations in gene expression and protein abundance underlying the observed lysosomal dysfunction (**Fig. S3A**). Filtering for lysosome-associated proteins resulted in the detection of 321 differentially expressed proteins (**Fig. 2A**). Surprisingly, the top-20 regulated lysosomal proteins (except for ANPEP) were not altered at a transcriptomic level (**Fig. 2B**). Next, we used a network medicine approach to further evaluate how these proteins are functionally related to each other. We identified the two podocyte-specific *GLA* KO modules for the respective up- and downregulated lysosomal proteins (**Fig. 2B, S3B-C**). The upregulated hits resulted in a smaller more specific module (64 proteins; z-score: 28). Gene ontology enrichment for cellular compartment and reactome pathways revealed an involvement of processes associated with membrane trafficking, autophagy, mitophagy and the lysosome in both modules (**Fig. S4A-B**). Molecular Function GO terms overrepresented in the disease modules were associated with proteins binding to phosphorylated residues and beta-adrenergic signalling kinases (**Fig. S4C**).

Strikingly, alpha-Synuclein (SNCA) was the only protein found as an upregulated protein by the SILAC-based proteome analysis but also by the network-based approach as a protein residing in the downregulated module, connecting both the upregulated and downregulated disease modules as a seed protein. SNCA binds to four out of the eight proteins that are connecting both modules with each other and the known interaction partners of SNCA are involved in autophagosome and lysosome function such as GABARAP1, MAPK1, LAMP2 and SQSTM1 (p62) (**Fig. 2C**).

One major degradation pathway for SNCA depends on the enzyme cathepsin D (30, 31), yet Fabry podocytes did not show cathepsin D activity (**Fig. 3A**). Treatment with recombinant aGAL over 96 hours mitigated and normalized the expression levels of all top ten upregulated lysosomal proteins except for SNCA (**Fig. 3B, Fig. S5**). Similarly, substrate reduction therapy using an inhibitor of glucosylceramide synthase did not result in a significant decrease of SNCA protein levels in our cell culture model, as well as in several organs of Fabry mice (**Fig. 3C & S6A-B**). In addition, also chaperone treatment did not change organ specific SNCA levels *in vivo*.

In human renal biopsies, SNCA was detected almost exclusively in the glomerular compartment, showing an increased expression in samples of untreated Fabry patients (**Fig. 3D**). SNCA staining intensity in biopsies of patients who underwent 5 years of ERT was partially reduced compared to baseline levels (**Fig. 3D**). Remarkably, we did not observe different SNCA levels in patient derived primary urinary cells and no induction through challenging these cells with globotriaosyl-sphingosine (lyso-Gb3) the main degradation product of Gb3 implicated in the disease's molecular pathology (**Fig. S7A-B**).

Modulating SNCA accumulation ameliorates Fabry podocytopathy

To elucidate the functional effect of alterations in SNCA levels in WT and aGAL deficient cells, we performed knockdown and overexpression analyses. We achieved a strong inhibition in both knockout and wild-type cells 48 hours after siRNA transfection (**Fig. 4A**). This inhibition was associated with a significant reduction in lysosomal area, lysosomal pH, and ROS accumulation (**Fig. 4B**) without complete reversal to wild-type levels. Next, a reverse overexpression of SNCA (**Fig. 4C**) induced pronounced alterations of lysosomal structure (**Fig. 4D**), and marked increases in lysosomal area, pH, and ROS production (**Fig. 4E**), mirroring the Fabry phenotype and confirming a central role of SNCA-signalling as a Gb3-independent mechanism of podocyte injury.

β 2 adrenergic receptor agonists as a novel therapy for Fabry podocytopathy

As SNCA pharmacological modulators are not currently available, we performed connectivity mapping analysis of the transcriptomic profile of Fabry podocytes, which identified the β 2 adrenergic receptor agonist Orciprenaline to be the top "anti-Fabry" compound with a relation score of -0,7 (**Fig. 5A** and **Table S2**). Indeed, Orciprenaline as well as another β 2 adrenergic receptor agonist, Clenbuterol, were able to significantly reduce SNCA accumulation in Fabry podocytes (**Fig. 5B**). Furthermore, Clenbuterol depicted a clear dose dependent effect on SNCA (**Fig. S8A-B**). In accordance with the effects of genetic SNCA reduction, β 2 adrenergic receptor agonist treatment resulted in decreased lysosomal area (**Fig. S9A**) and increased lysosomal acidification in knockout podocytes (**Fig. S9B**). Strikingly, the combination of ERT and Clenbuterol showed an additive effect on the restoration of LAMP1 accumulation (**Fig. 5C**) and lysosomal pH (**Fig. 5D**) and ROS production (**Fig. 5E**) in Fabry podocytes, mirroring ultrastructural findings (**Fig. S9C**).

Discussion

The pathomechanisms of FD, specifically Fabry nephropathy, remain incompletely understood due to several factors. First, the mutational landscape is heterogeneous, as classical hot-spot mutation regions are not commonly observed and no clear genotype-to-phenotype correlations have been described (32).

Furthermore, established animal models fail to recapitulate the hallmarks of Fabry nephropathy besides tubular substrate inclusions (24, 25, 33).

In this context, our study contributes to a better understanding of Fabry pathophysiology through the deep phenotyping of a complete *GLA* knockout in podocytes (27) eliminating residual intact and functional enzyme (34, 35). On a functional level, the drastic lysosomal phenotype with decreased acidification, accumulation of ROS and increased autophagy matches observations made in previous studies and other lysosomal storage diseases (35–37), such as previous reports in primary fibroblasts derived from Gaucher patients (38) and endothelial cells exposed to Gb3 (39). However, in contrast to fibroblasts (40) mitochondrial dysfunction did not exert a decisive role in podocytes indicating disease and cell-type specific pathologic pathways may be involved in different lysosomal storage disorders (41). This is also in agreement with recent finding that podocytes are being maintained by anaerobic glycolysis as the predominant metabolic pathway (42).

The primary enzymatic defect and subsequent substrate depositions altered the overall transcriptomic and proteomic landscape of *GLA* KO podocytes confirming recent reports (43–46). Interestingly, we observed increased levels of GBA protein, as well as other well described lysosome associated proteins such as LIMP2 (encoded by the gene *SCARB2*). The latter has been shown to serve as a specific receptor for glucocerebrosidases and to be involved in proper lysosomal biogenesis (45, 47), suggesting that lysosome impairment extends beyond the initial enzyme defect. In this context, the identification of SNCA as a central player in lysosomal dysfunction resistant to currently available therapies in our cell line, a Fabry mouse model and patient biopsies reaffirms the existence of an additional mechanism of injury in FD. In a reverse approach primary urinary cells of Fabry patients did not depict increased SNCA levels upon Gb3 stimulation, moreover, indicating a substrate independent mechanism as a cause of SNCA accumulation.

SNCA is produced in many cells and constantly degraded through chaperone-mediated autophagy (48) and cathepsin degradation (49). This protein has been implicated in other lysosomal storage diseases (50) and is well-known in synucleinopathy related neurodegenerative diseases such as Parkinson disease (51, 52), where SNCA is proposed to form a negative feedback loop that leads to decreased enzymatic degradation (53–55). Importantly, the aggregation of pathological SNCA isoforms has been reported as toxic to cells (56–58), and the modulation of SNCA-signalling reverses lysosomal clustering (59), suggesting that SNCA accumulation may represent an intriguing therapeutic target for FD (60).

In agreement with previous reports (13, 14, 61, 62), ERT significantly reduced the volume of podocyte specific Gb3 inclusion bodies in follow-up biopsies, but without amelioration of podocyte injury and with little effect on glomerular SNCA accumulation. Hence, despite significant reductions in Gb3 accumulation upon ERT and reported correlation of foot process width to Gb3 inclusions (62), remaining Gb3 or substrate independent mechanisms lead to persistent end-organ damage (63). In this context, our data regarding SNCA accumulation provide a potential explanation to the clinical observations, as they confirm a substrate independent pathomechanism, and challenge the adequacy of the current standard care for patients with FD.

We believe that our findings have direct clinical implications, as conventional therapy may not be sufficient to prevent and reverse end-organ damage if not initiated very early or accompanied by additional strategies (64, 65). In our study, connectivity mapping identified beta-adrenoreceptor agonists as potential FD

modulators (66, 67). Interestingly, it has been reported that beta-2-agonists decrease the risk of Parkinson disease via epigenetic downregulation of SNCA gene transcription and protein reduction (68) and beta-2-adrenoreceptor signalling was previously described in podocytes (69). We confirmed the positive effects of beta-2-agonists treatment on lysosomal size, function and cellular SNCA levels mirroring the effects of siRNA mediated SNCA reduction. This is the first report to delineate a positive effect by targeting pathways outside the sphingolipid metabolism in Fabry podocytopathy. However, it should be noted that beta-2-agonists will have limited therapeutic potential in FD, as Fabry cardiomyopathy renders patients prone to arrhythmias which could be potentiated through beta-2-agonist treatment. Despite of this, the pharmacological amelioration of lysosomal dysfunction through SNCA reduction serves as an ideal proof-of-concept, indicating that novel strategies could serve as additional therapies and future studies might also elucidate non-arrhythmogenic downstream signals of beta-2-adrenoreceptor signalling controlling SNCA levels (70).

The observed cell-type specific accumulation of SNCA in the kidney of Fabry patients should be a further indicator to investigate shared pathomechanisms in lysosomal storage diseases. Notably, a subset of Gaucher disease patients develops Parkinson disease-like conditions mainly due to SNCA cellular accumulation (71), which has been attributed to decreased autophagosomal flux, defective mitophagy, and impaired lysosomal function due to *GBA* mutations (50, 72–74). First evidence has been provided through both a survey and an observational study drawing a link between Fabry and Parkinson's disease (60, 75). Similarly, *Gla* knockout mice present with SNCA accumulation in the Pons region of the brain in later stages of life (76). Future work may identify to what extent lysosomal dysfunction results in organ-specific phenotypes in different lysosomal storage diseases

It is possible that additional mechanisms in Fabry podocytopathy remain uncovered as podocytes in culture tend to partially lose their *in vivo* expression profile (77). However, the clear accumulation of SNCA deposits detected in glomeruli of Fabry patients, depicts the translational aspects of our cell culture model and the remaining glomerular SNCA deposits after years of therapy provide an explanation why already existing glomerular damage cannot be reversed but only its progression slowed (9–11). While beta-2-agonist drugs with their pro-arrhythmogenic potential will not be a therapy choice in multi-organ affected Fabry patients, early conventional therapy initiation to prevent further accumulation of Gb3 and concomitant cell/organ dysfunction will remain of key importance (78). However, as proven by this study, the complementation with novel pathway targeted therapeutic strategies will have the potential to significantly improve long-term outcomes of our patients.

In conclusion, our study systematically maps the signalling networks of Fabry-associated podocyte disease, identifies the role of SNCA to lysosomal impairment and disease severity in Fabry disease, and conceptually proposes a novel additive pharmacological targeting strategy aiming to halt and reverse Fabry nephropathy.

Methods

Quantification of Gb3 deposition and foot process width in renal biopsies

Subjects consisted of eight (M/F=7/1) patients with classic Fabry disease. Fabry disease was confirmed by measurement of leukocyte alpha-galactosidase A activity and/or *GLA* sequencing. Studies were performed in accordance with

principles of the Declaration of Helsinki and were approved by the Institutional Review Board of the University of Washington, University of Minnesota, and the Regional Ethics Committee of Western Norway. Written informed consent had been obtained from each subject.

Renal biopsies were performed as part of a clinical trial protocol (ClinicalTrials.gov#: NCT00196716) or standard of care before the initiation of enzyme replacement therapy and 11 (n=6) or 12 (n=2) months following treatment with agalsidase-beta (1 mg/kg/every other week). Kidney biopsies from none living transplant donors obtained before organ removal were studied as controls. Semi-thin sections of 2.5% glutaraldehyde-fixed, plastic embedded tissues were stained with toluidine blue for identification of glomeruli. Random glomerular sections were prepared for stereological studies as described elsewhere (62). Overlapping digital low-magnification (~8000X) images of entire glomerular profiles and high-magnification (~30,000X) images of glomeruli according to a systematic uniform random sampling protocol were obtained using a JEOL 1010 electron microscope (61). Volume of GL-3 inclusions per podocyte [$V(\text{Inc}/\text{PC})$] was estimated using a combination of point counting and point-sampled intercept method (21, 62). Podocyte average foot process width (FPW) was estimated as the reciprocal of slit-length density as previously described (79).

Cell culture

Conditionally immortalized human podocytes were kindly provided by M. Saleem (University of Bristol, UK). Cells were let to proliferate at 33°C in RPMI-1640 medium supplemented with 10% fetal calf serum (FCS), Penicillin/Streptomycin, ITS and non-essential amino acids. To induce differentiation, 70% confluent podocytes were switched to 37°C for 10 to 14 days (unless indicated otherwise). Cells were let to differentiate over collagen IV coated plates (50 ng/ μl , Sigma, Germany) in all experiments. Rescue experiments were performed by adding 20 $\mu\text{g}/\text{ml}$ alpha-galactosidase-A (Sanofi – Paris, France) to the complete medium. aGAL treatment was applied on 10 days differentiated cells over 96 hours with 24 hours' intervals of enzyme renewal. Venglustat was administered at 300nM concentration on 8 days differentiated cells over 120 hours with 24 hours' intervals of compound renewal. The β_2 adrenergic receptor agonist Clenbuterol hydrochloride (European Pharmacopoeia) and Orciprenaline (Sigma Aldrich) were used in our experiments. Different concentrations were applied over 96 hours (as indicated in the figure legends). Likewise, alpha-GAL, β_2 adrenergic receptor agonist treatment was applied on 10 days differentiated cells and renewed every 24 hours over 96 hours. Primary urinary cells were collected from Fabry patients in the International Center for Lysosomal Storage Diseases (ICLD) Hamburg according to Ethics Statement PV3501 approved by the Ethics Board of the Board of Physicians Hamburg. Cells were taken into culture and expanded as described previously (45, 80). After reaching a sufficient confluency, cells were treated with normal proliferation medium (80) supplemented with DMSO (Vehicle) or 100 nM lyso-Gb3 (Sigma Aldrich) in DMSO for 48h.

Generation of isogenic GLA knockout human podocytes

CRISPR/Cas9 genome editing was applied to generate *GLA* knockout podocytes *in vitro* as previously described (81). Briefly, CRISPR/Cas9 genome editing with two different gRNAs (guideRNA1: 5'-TTGTCCAGTGCTCTAGCCCC (AGG)-3', guideRNA2: 5'-CAGTGCAGCCAGCCCATGGT (AGG)-3' targeting the first exon of the human *GLA* gene was used. A web-based platform was operated in order to design these gRNAs (e-crisp.org - <http://www.e-crisp.org/E-CRISP/>). The gRNAs being

subcloned in targeting CRISPR nuclease vectors with OFP (GeneArt life technologies, Carlsbad, CA, USA) according to the manufacturer's protocol were inserted in the immortalized human podocytes via electroporation. Mixed cell populations were validated with restriction enzyme digestion with NcoI (5'-C||CATGG-3', New England BioLabs Inc., Ipswich, MA, USA) for gRNA2 or with an indel mutations detecting and cleaving the enzyme (Genomic Cleavage Detection Kit, GeneArt life technologies, Carlsbad, CA, USA) for gRNA1. After an incubation period of 48 hours, single cells were selected via FACS, sorted into 96-well plates, and further expanded into isogenetic clone colonies. The DNA sequences were analysed using the Sanger technique after initial DNA isolation and amplification (forward primer: 5'-TGGAAATAGGGCGGGTCAAT-3', reverse primer: 5'-TTCCCCAAACACACCCAAAC-3'). The sequencing results proved the sex of the clone cell line used to be male. Hemizygous *GLA*-clones translated in silico were reviewed for frameshift mutations and premature stop codons.

Electron microscopy of cell culture podocytes

Cell samples were fixed in 4% paraformaldehyde plus 1% glutaraldehyde in 0.1M phosphate buffer over night. After contrastation using 1% osmium tetroxid in 0.1 M phosphate buffer (45 min at RT) and 1% uranyl acetate (in 70% ethanol, RT) samples were dehydrated in an ascending ethanol series and embedded in epoxy resin (Durcupan, Sigma Aldrich). Ultrathin sections of approx. 70nm thickness were prepared using a Leica Ultracut UC6. For imaging a Philipps CM100 transmission electron microscope was used.

RNA sequencing

Conditionally immortalized human podocyte WT and CRISPR/CAS9 *GLA* KO cell lines were differentiated at 37°C at 70% confluency for 10 to 14 days. Total RNA of cells was isolated using the Phenol/Chloroform method as previously described (82).

Library preparation and sequencing was performed by GATC, Germany. All raw data was deposited to Gene Expression Omnibus (GEO), accession number GSE186258.

Connectivity mapping

The top 100 up and downregulated genes from RNA Sequencing data were uploaded to the next generation connectivity mapping tool (CLUE website) (67). Output analysis and ranking were automatically performed by the website.

Proteomics analysis

In order to identify new regulators that may play a role in the lysosomal dysfunction we studied the whole proteome in *GLA*-KO cells by employing quantitative, SILAC-based proteomics and our novel podocyte Fabry model and by analysing 3 Fabry clones versus 3 WT clones. For MS analysis, SILAC labeling of human immortalized podocytes was performed for 14 days as previously described (83). Based on SILAC labeling and protein concentration WT and KO samples were mixed 1:1 for MS-analysis. LC-MS/MS data analysis was performed as reported before (Weise et al., Mol Neurobiol, 2019). The MS raw data files were uploaded into the MaxQuant software version 1.4.1. which performs peak and SILAC-pair detection, generates peak lists of mass error corrected peptides and data base searches. We identified nearly 2,300 proteins among which 321 are lysosomal

enriched proteins. The top 10 up and downregulated were considered as targets of high interest for further functional analysis. All raw data and original result files were deposited to the ProteomeXchange Consortium (<http://proteomecentral.proteomexchange.org>) via the PRIDE partner repository with the dataset identifier PXD029618.

Building GLA specific network modules

Network-based approaches are based on the assumption that proteins that participate in the same biological processes or share molecular functions are not scattered randomly but tend to cluster and build functionally relevant modules within the human interactome. In order to identify the *disease module* that connects the detected up- and downregulated proteins associated with *GLA* knockout, we used a large dataset of known protein interactions recently compiled by Cheng and colleagues (84). It consists of 16,677 proteins (nodes) connected by 243,603 protein interactions (edges). One way to build the module would be to search for known direct interaction partners of the up- and downregulated proteins (seed proteins), calculate the size of the resulting largest connected module between them and evaluate whether this size significantly differs from random expectation. However, this method would favour highly connected proteins in the human interactome. In order to detect connections between the seed proteins in an unbiased way, we used a recently published disease module detection algorithm (DIAMOnD). DIAMOnD takes into account the *connectivity significance* of proteins to a set of seed proteins and helps to build a module around them (85) The algorithm calculates the probability that a protein with k links has exactly k_s links to the seed proteins using the hypergeometric distribution and determines the p-value that it has more connections to the seed proteins than expected. The protein with the lowest p-value is then added to the module and a new iteration starts. Since the algorithm could iterate over all 16,677 proteins of the interactome a break-off criterion to determine the final optimal module size needs to be defined.

Determining the final module size

In order to determine the final module size we used the method that was recently described by Halu and colleagues (86). DIAMOnD ranks the proteins that are not seed proteins according to their p-value (see above) and incorporates the protein with the lowest p-value into the module. After each iteration the resulting module size, e.g. the number of nodes that are directly connected to each other is determined, and compared against random expectation (1000 random network samples), resulting in a respective z-score:

$$z - score = \frac{module - randommodule}{\sigma_{random}},$$

where *module* and *randommodule* are the sizes of the resulting largest connected module and the random expectation. The standard deviation of the calculated 1000 random module sizes is depicted by σ_{random} . After each iteration, we determined how many seed proteins are integrated into the module. As proposed by Halu et al. the module size where all seed proteins are integrated into the module and where the corresponding z-score is above 1.96 (significant z-score) is taken as the final module size.

aGAL enzyme activity measurement

The fluorometric measuring method of the enzyme activity of alpha-galactosidase-A with 4-Methylumbelliferyl- α -D-galactopyranoside has been previously fully

described (87–89). In addition, N-acetylgalactosamine has been shown to significantly inhibit alpha-galactosidase B activity (89). Briefly, cells from several *GLA*-KO isogenetic clones and wildtype cells were counted and pelleted. The pellets were lysed in 500µl lysis buffer (27 mmol/l sodium citrate, 46mmol/l sodium phosphate dibasic, 0,1% Triton X-100, 1 M HCL, in ddH₂O, pH 4,6) by pipetting on ice. Proteins were then separated by centrifuging at 13,2 g and the protein concentration was determined via the Pierce BCA protein assay. 10µl of each sample with three technical replicates were incubated with 25µl test buffer (27 mmol/l sodium citrate, 46 mmol/l sodium phosphate dibasic, 6 mmol/l 4-Methylumbelliferyl α-D-galactopyranoside, 90 mmol/l N-Acetyl-D-galactosamine, 1 M HCL, in ddH₂O, pH 4,6) at 37°C for one, six or eleven hours. Subsequently, 35 µl stop buffer (0,4 mol/l Glycine, 5 N NaOH, in ddH₂O, pH 10,8) was added and the fluorescence measured. After initial shaking with amplitude of 1 mm for 10 seconds and a 25-time excitation with 355nm the emission of 455nm were measured over an integration period of 20 µs. A standard activity curve was established using aGAL from green coffee beans (Sigma-Aldrich, Saint Louis, MO, USA) with known aGAL activity in serial dilution.

Mass-spectrometric measurement of Gb3

Differentiate WT and KO podocytes were treated 48 hours with alpha-GAL or PBS for mass-spectrometric Gb3 quantification as described previously (90). By the end of incubation, cells were washed twice with PBS, harvested by trypsin and washed again with ice-cold PBS and directly lysed in 0.2% Triton-PBS. Equal volume was taken from each sample for total protein measurement in order to normalize the final readings (Pierce BCA protein assay). Lysate was then stored at -20 and GB3 quantification were performed by pharm-analyt Labor GmbH, Austria.

Lyso-GB3 solid phase extraction:

For solid phase extraction 40 µL of the plasma sample were diluted in 320 µL water/Acetonitrile/MeOH(final: 1:2:2) and 36 µL 1M HCl in an 1.5 mL reaction tube. Cells were resuspended in 360 µL of water/Acetonitrile/MeOH (1:2:2), followed by homogenization and lysis at -20 degrees for 2h. For solid phase extraction, Oasis MCX 1 cc Vac cartridges, 30 mg Sorbent, 60µm (Waters Corp., Milford, MA) were used along with a vacuum manifold and pump. The cartridges were activated with 1000 µL MeOH 100% and then 1000 µL 1M HCl. Then, the samples were loaded. Columns were washed with 1000 µL HPLC grade water + 2% formic acid and afterwards with 1000 µL MeOH + 0.2% formic acid. The lipids were eluted with 600 µL MeOH + 2% NH₄OH and excess solvent was evaporated (CentriVap® Concentrator Labconco, Kansas City, Missouri) at 10° C. After evaporation the eluate pellets were resuspended in 50 µl 1:1 ACN and water + 0.2% formic acid , centrifuged at 18000 xg, 4°C for 10 minutes and the supernatant was transferred into analytical vials for the LC-MS measurement.

Lyso-GB3 LC-MS analysis:

Targeted metabolomics analysis was performed on a triple-quadrupole (Agilent Triple Quadrupole 6495C, San Diego, CA) coupled with an ultra-high pressure liquid chromatography system (1290 Infinity, Agilent Technologies). Data acquisition was done with Agilent MassHunter Workstation Data Acquisition (Version 10.1). Samples were separated on a BEH amide column (1.7 µm, 2.1 x 100mm) (Waters, Taastrup, Denmark) with buffer A (HPLC grade water with 20mM ammonium formate + 0.1% formic acid) and buffer B (ACN + 0.1% formic acid).

For separation the following gradients (A/B) were used with a flow rate of 0.4 mL/minute: T0 10/90, T1 35/65, T4 35/65, T6 50/50, T8.5 10/90, and T12.5 10/90. 2 μ L of the sample were injected each run. Multi reaction monitoring was used as the scan type. The transition list and retention times for measured Lyso-GB3 were: 786.45 \rightarrow 282.2 (quantifier) 786.45 \rightarrow 264.2 (qualifier). The collision energies (MS2 or quantifier and qualifier ion transitions) were optimized. ESI source parameters were: Gas temperature = 180° C, gas flow = 12L/minute, Nebulizer = 20 psi, sheath gas = temperature 200° C, sheath gas flow = 12 L/minute, cap voltage = 4000 V, and nozzle voltage = 1500 V.

Dual-emission ratiometric measurement of lysosomal pH and LysoTracker

LysoSensor™ Yellow/Blue DND-160 (Life Technologies) was used according to the manufacturer description in order to determine the lysosomal acidity in cultured cells. Briefly, cells were suspended and labelled with 10 μ M LysoSensor DND-160 for 2 hours at 37°C in 10% medium, cells were then pelleted and washed in PBS twice. The labelled cells were treated for 10 min with 10 mM monensin (Sigma) and 10 M nigericin (Sigma) in 25 mM 2- (N-morpholino) ethanesulfonic acid (MES) calibration buffer, pH 3.5–8.0, containing 5 mM NaCl, 115 mM KCl and 1.2 mM MgSO₄. Cells were then distributed in black 96-well plate (2500cells/well) and the fluorescence was measured with a TECAN plate reader. Light emitted at 440 and 535 nm in response to excitation at 340 and 380 nm were measured, respectively. The ratio of light emitted with 340 and 380 nm excitation was plotted against the pH values in MES buffer, and the pH calibration curve for the fluorescence probe was generated (91). In order to study the lysosomal structure and to score the cellular lysosomal mass, LysoTracker™ Red DND-99 (Life Technologies) was used according to the manufacturer's recommendation. LysoTracker was applied to differentiated podocytes for 30min at 37°C with a final working concentration of 50 nM. Cells were washed and images were taken using a Zeiss Axio Observer microscope, equipped with a 63x objective and Apotome function and analysed using cell profiler. The Lysosomal fraction was blotted as a percentage of lysosomal to cellular area.

Oxidative Stress Detection

DCFDA-Assay (ThermoFisher Scientific) was employed to measure ROS level in adherent cells (92). Differentiated cells were harvested and seeded back in a dark, clear bottom 96-well microplate with a concentration of 2500 cells per well and allowed to adhere overnight. Cells were then washed with PBS and incubated with DCFDA solution (20 μ Mol in PBS supplemented with Ca²⁺ & Mg²⁺) by adding 100 μ l/well for 45 minutes at 37°C in the dark. DCFDA Solution was removed, and wells were washed twice with PBS and the fluorescence was immediately measured by TECAN reader (Ex/Em= 485/535 nm).

Thin layer chromatography

Lipid extraction was carried out in principle according to the method of Bligh and Dyer (93). Pelleted cells were lysed by osmotic shock using ddH₂O, afterwards transferred into a glass tube, mixed and vortexed with chloroform:methanol (1:2) for 1 min. Then, 1.25 mL of chloroform and 1.25 mL of ddH₂O were added and mixed for 15 sec. For phase separation, the solution was centrifuged at 3000 rpm for 10 min at 15°C. The organic phase was transferred to a new glass tube. The hydroalcoholic phase was washed once with 1.5 mL of chloroform, mixed for 15 sec and then centrifuged at 4000 rpm for 10 min at 15°C. The organic phases were

combined and the solvent was evaporated under a stream of nitrogen. Dried lipids were either stored under an argon atmosphere or resolved in chloroform:methanol (2:1) for thin-layer chromatography (TLC). Lipid extracts were loaded on two silica plates and separated by TLC using methanol:chloroform:ddH₂O (60:35:8) as a mobile phase. Afterwards one silica plate was incubated with p-anisaldehyde/acidic alcohol solution and placed in an oven for 15 – 30 min at 120°C to stain overall lipids. For specific detection of Gb3, the other plate was fixed by 3.75 % (w/v) polyisobutylmethacrylate/n-Hexane, blocked with 1% (w/v) BSA/PBS (containing calcium and magnesium), incubated afterwards with biotinylated Shiga toxin B-subunit (1.8 µg/mL) and subsequently with alkaline phosphatase-conjugated streptavidin (2 µg/ml). Gb3 bands were visualized by a colorimetric reaction with NBT/BCIP Substrate Solution (Thermo Scientific). The chromatogram was densitometrical analysed and documented using Fusion FX (Vilber Lourmat) and ImageJ software.

Seahorse XFp mitochondrial analysis and ATP measurement

Optimization of cell density for human podocytes of the respective genotype as well as optimization of the working concentration titers for each individual inhibitor was conducted prior to the Seahorse XFp experiments according to the manufacturer`s instructions (Agilent Technologies). Human podocytes were seeded at a density of 15 000 cells/well. The Seahorse XFp Mito Stress Test was performed following the manufacturer`s instruction. Specifically, podocytes were seeded on XFp microplates 24h before the experiment. On the day of the assay cells were rinsed and XF assay buffer was added for further equilibration. Afterwards the plate was incubated for 1 h at 37°C in a non-CO₂ incubator. All medium and solutions of mitochondrial complex inhibitors were adjusted to pH 7.4 prior each assay. Following four baseline measurements of OCR and ECAR, for Mito Stress Test inhibitors of the respiratory chain were sequentially injected into each well. Three OCR and ECAR readings were taken after addition of each inhibitor and before automated injection of the subsequent inhibitor. Mitochondrial complex inhibitors, in order of injection, included oligomycin (1.5 µM) to inhibit complex V, FCCP (1.0 µM) to uncouple the proton gradient, antimycin A (1.0 µM, inhibitor of complex III), and rotenone (1.0 µM, complex I inhibitor). OCR and ECAR were automatically calculated by Seahorse XFp software version 2.2.0 (Seahorse Bioscience, Billerica, MA, USA). After each experiment podocytes were fixed with paraformaldehyde and nuclei were stained with DAPI. Olympus ScanR Screening Station for high-throughput microscopy detection (Olympus, Tokyo, Japan) was used for assessment of cell number to normalize XFp analysis data.

SNCA knockdown and over-expression in immortalized human podocytes

Generation of siRNA mediated knockdown of SNCA in immortalized human podocytes was performed using the following sequences: T1-1: 5'-CAUAGUCAUUUCUAAAAGUUU-3' T2-1: 5'- GGAUUUAUGUGGAUACAAAUU -3'. These sequences have been previously tested and published (94). Transfections were performed using Amaxa nucleofector technology (Lonza, Basel, Switzerland) according to manufacturer`s instructions. Cells were let 10 days to differentiate prior transfection and seeded back for 48 or 72 hours prior analysis. The knockdown efficiency was compared to scramble transfection using western blot 48 and 72 hours post transfection.

Western blot and immunofluorescence

The buffers, the systems and the protocols that were applied in western blotting can be found in our previous publication (95). The following anti-bodies were used in WB experiments: α -Galactosidase (OriGene Technologies - TA336243), α -tubulin (Sigma-Aldrich - T9026), Actinin 4 (Abcam - ab108198), p62 (Cell Signaling Technology - 5114), LC3 (Invitrogen - PA1-16931), SNCA (Santa Cruz Biotechnology - sc-12767), SCARB2 (Lifespan Biosciences - LS-B3225-0.05), TTYH3 (Origene - TA339554), MFEG8 (Sigma-Aldrich - HPA002807), CD63 (Proteintech - 25682-1-AP), DDP (Novus Biologicals - H00001678), PLSCR3 (Abcam - ab57554), GBA (Abcam - ab96246) and ITM2B (Abcam - ab119044). TOM20 (Santa Cruz Biotechnology - sc-11415) and LAMP-I (Abcam - ab24170) were used for immunofluorescence staining. Immunofluorescence staining was performed on differentiated cells seeded in collagen IV 8-well chamber slides (Ibidi, Germany). Cells were fixed in 4% paraformaldehyde in PBS for 10 minutes and permeabilized using 0.1% Triton X-100 in PBS for TOM20 and Methanol for LAMP-1. Permeabilized cells were washed in PBS and blocked with 5% BSA in PBS for 1h at room temperature. Primary and secondary antibodies were diluted in blocking solution and incubated for 120 minutes and 45 minutes respectively. Z-stack images of TOM20 and LAMP1 stained cells were acquired and presented as maximum intensity projections in respective figures.

Immunostaining of SNCA

Kidney biopsies before the onset of ERT and after five years of treatment were taken from a selection of a larger patient series already described elsewhere (96). Paraffin sections of 3 μ m thickness were cut and incubated at 42°C overnight. Sections were then deparaffinized and rehydrated (20 min xylene, 10 min 100% ethanol, and 5 min in 95%, 85%, 75% and 50% ethanol). Slides were washed for 5min in (PBS 1X-tween 0,1%). Antigen Retrieval Solution (pH6) was used in steam cooker for 30 min and the slides were let to cool for 20 min on ice. Slides were washed 3 times with PBS and blocked with 5% BSA in PBS for 45 min. Endogenous peroxidase was inactivated with DAKO peroxidase inhibitor for 15 min. Primary antibody - SNCA (Santa Cruz Biotechnology - sc-12767) - was diluted in blocking solution (1:200) and the samples were incubated for 2 hours at room temperature. Goat anti-Rabbit Biotinylated - DAKO (1:500) was added for 30 min and Streptavidin\HRP- DAKO (1:500) for 30 min followed by ACE substrate\ DAKO for 10min. Slides were washed after every step with PBS1X. Finally, slides were mounted using permanent mounting medium. Stained slides were scanned with the Aperio ScanScope XT system (Leica Biosystems Imaging, Wetzlar, Germany) at \times 40 objective magnification and viewed in eSlide Manager (Leica Biosystems Imaging, Wetzlar, Germany). Staining intensities of SNCA were analyzed with the color deconvolution method(97). Percent total positive pixel count was acquired with the Aperio Color Deconvolution algorithm v9 (Leica Biosystems Imaging, Wetzlar, Germany) from annotated glomerular regions.

In-cell western for SNCA

Primary urinary cells were grown in a 0,1% Gelatine (Millipore Sigma) coated 96well plate until confluent. After treatment with Vehicle / lyso-Gb3, cells were washed in PBS, fixed in 4% Paraformaldehyde, washed again in PBS and blocked/permeabilized in 5% BSA, 0,1% Triton X-100 in PBS for 1h at room temperature. After 3 washing steps in PBS, cells were stained with primary antibody (Sigma-Aldrich - HPA005459) 1:200 overnight. The next day, after 3 additional washing steps in PBS, cells were incubated in secondary antibody (LICOR IRDye 800cw) 1:200 and Draq5 nuclear stain (Abcam - 108410) 1:1000 or

1h at room temperature. Cells were washed again 3 times and imaged at the LICOR Odyssey imager at 3µm focus, 89µm resolution.

Mouse line and in vivo treatment

hR301Q α-Gal A Tg/KO mice (Tg/KO) were used as a model of Fabry disease(98). Specifically, these mice are homozygous for endogenous *Gla* knock-out and express the human transgene *GLA* carrying the R301Q mutation under the transcriptional control of the human *GLA* promoter. 6 months old homozygous Tg/KO mice were treated with 1-deoxygalactonojirimycin (migalastat, obtained from Amicus Therapeutics – Philadelphia, USA) or with ibiglustat (Venglustat, obtained from Cayman Chemical Company) at the same dose of 100 mg/Kg/day (5 mice per group). Both Migalastat and Venglustat were administered orally to mice in drinking water. The appropriate concentration of drugs in drinking water was determined based on the average daily water consumption of Fabry Tg/KO mice (~5 ml/day per mouse), and the solutions were made fresh weekly. Migalastat treatment was administered in alternate months (98) while Venglustat was administered continuously from 6 to 9 months of age. Control Tg/KO mice and C57BL/6 wild type mice were exposed to DMSO (vehicle) in a 1:1500 dilution in drinking water. At study completion, mice were euthanized, and the organs of interest (Heart, kidney, liver, and brain) were quickly removed, rinsed in cold phosphate-buffered saline (PBS), and immediately frozen in liquid nitrogen for subsequent analysis.

SNCA ELISA

Human and murine SNCA were determined using the Human Alpha-synuclein ELISA (Abcam – ab260052) or Mouse Alpha-synuclein ELISA (Abcam – ab282865) according to the manufacturer's protocols.

Cathepsin Activity Assay

Cathepsin D activity was determined according to Huarcaya et al (49). In short, cells were lysed in acidic buffer (50 mM sodium acetate, 0.1 M NaCl, 1 mM EDTA, 0.2% Triton X-100, pH 4,5) and 2µg incubated 0.1 µM quenched fluorogenic peptide (Enzo, BML-P145) and 0.025 mM leupeptin (Enzo, ALX-260-009-M025) at 37°C for 30 min in 100µl additional lysis buffer. Afterwards samples measured using 322nm excitation and 381nm emission.

Statistics and reproducibility

Data are expressed as scatter or violine plots. Paired Student's t-test or ONE-WAY Anova (multiple comparison test - Tukey) were used based on data distribution. Statistical significance was defined as *P<0.05, **P<0.01, ***P<0.001 and ****P<0.0001, n.s. - not statistically significant. Number of independent experiments and total amount of analysed cells are specified in each figure.

Ethical approvals

Patients in this study provided written informed consent Renal biopsies were performed as part of a clinical trial protocol (ClinicalTrials.gov#: NCT00196716) or standard of care before the initiation of enzyme replacement therapy.

Ethical permission was granted from the ethics committee of the Western Regional Health Authority in Norway (REK Vest no. 2010/2483). Informed consent was signed by the patient and/or their designees in all cases. Kidney biopsies from the

Norwegian Kidney Biopsy Registry with normal light- or electron-microscopical appearance served as controls (REK Vest no. 2013/553).

Animal husbandry and all experiments were conducted under Institutional Animal Care and Use Committee-approved protocols at Federico II University.

Data availability

The RNA-Seq and proteome data reported here are deposited in the NCBI's Gene Expression Omnibus (GEO) database and ProteomeXchange Consortium (GEO GSE179975 & PXD029618).

Author contributions

TBH initiated this study. FB and AA designed the research study, conducted experiments, acquired data, analysed data and wrote the manuscript. FB was chosen as first co-first author for the planning and coordination of the revision process and the revision of the manuscript. DS, MRo, MW, OE, NW, JG, SDL, FH, MNW, BD, PR, AM, WS, KC, SWG, OK, OH, TB, FG, WL, TE, WR, CT and BN conducted experiments, acquired data and analysed data. NM and MM provided resources and acquired patient samples. ACM, KS, AH and CMS provided resources and revised the manuscript. HPM, CMS, GI & MMR designed the research study and provided resources. VGP, CS & TBH designed and supervised the research study, provided resources, wrote and revised the manuscript.

Acknowledgements

We thank Charlotte Meyer, Betina Kiefer, Valerie Oberüber and Anja Obser for expert technical assistance. We thank Prof. Em. Einar Svarstad for taking part in the treatment and recruitment of Fabry patients. The hR301Q mice of the Naples mouse cohort were provided through AMICUS Therapeutics. This study was supported by the 3R (Replace, Reduce, Refine) Start-up Funding Program, awarded by the Medical Faculty Hamburg in 2018 to Fabian Braun and Arne Hansen. We would also like to express our gratitude to all members of our laboratories and to the Life Imaging Center (LIC) of the University of Freiburg for helpful discussions and support.

Funding

FB was supported by the Else Kröner Fresenius Stiftung (2021_EKMS.26) & the German Society of Nephrology. DS was supported by Else Kröner-Fresenius-Stiftung grant 2014_MOTIVATE. AM and NW was supported by the Deutsche Forschungsgemeinschaft DFG (CRC1192). JG is supported by PON (Ramp;I 2014-2020), from "REACT-EU" IV.4 action, WR acknowledges support by a starting grant from the European Research Council (Programme "Ideas," ERC-2011-StG 282105), and by the Deutsche Forschungsgemeinschaft (DFG, German Research Foundation) under Germany's Excellence Strategy (EXC-294 and EXC-2189). CMS was supported by the DFG (ME2108/10-1, INST 152/696-2, SFB1192, project B3), GI is supported by PRIN (2017HTKLRF), from the Italian Ministry of Research, WR and CS was supported by the German Research Foundation (DFG—Deutsche Forschungsgemeinschaft) ((SCHE 2092/1-2, SCHE 2092/3-1, SCHE 2092/4-1 (RP9, CP2, CP3) (project-IDs 241702976 and 438496892); CRU329 to C.S. (project-ID 386793560); CRC1453 (project-ID 431984000); CRC1160 (project-ID 256073931)); by the MatrixCode research group by FRIAS, Freiburg, the Excellence Initiative of the German Federal and State Governments, the German Society of Nephrology DGFN, the Else Kröner Fresenius Stiftung, NAKSYS and by

the Berta-Ottenstein Programme, Faculty of Medicine, University of Freiburg. TBH was supported by the DFG (CRC 1140 (KidGen), CRC1192, HU 1016/8-2, HU 1016/11-1, HU 1016/ 12-1), by the BMBF (STOP-FSGS- 01GM2202A, NephRESA-031L0191E and UPTAKE- 01EK2105D), by the Else-Kröner Fresenius Foundation (Else Kröner-Promotionskolleg –iPRIME), by the European Research Council-ERC (grant 616891) and by the H2020-IMI2 consortium BEAt-DKD (115974); this joint undertaking receives support from the European Union's Horizon 2020 research and innovation program and EFPIA and JDRF.

Conflict of interest

The authors declare no competing interests.

References:

1. Anderson W. A CASE OF "ANGEIO-KERATOMA."*. *British Journal of Dermatology* 1898;10(4):113–117.
2. Kuech E-M, Brogden G, Naim HY. Alterations in membrane trafficking and pathophysiological implications in lysosomal storage disorders. *Biochimie* 2016;130:152–162.
3. Guce AI et al. Catalytic mechanism of human alpha-galactosidase.. *J Biological Chem* 2009;285(6):3625–32.
4. Schiffmann R. Fabry disease.. *Handbook of clinical neurology* 2015;132:231–248.
5. Mehta A et al. Natural course of Fabry disease: changing pattern of causes of death in FOS - Fabry Outcome Survey.. *J Med Genet* 2009;46(8):548–52.
6. Schiffmann R et al. Enzyme Replacement Therapy in Fabry Disease. *Jama* 2001;285(21):2743.
7. Eng CM et al. Safety and efficacy of recombinant human alpha-galactosidase A--replacement therapy in Fabry's disease.. *The New England journal of medicine* 2001;345(1):9–16.
8. Germain DP et al. Treatment of Fabry's Disease with the Pharmacologic Chaperone Migalastat.. *The New England journal of medicine* 2016;375(6):545–555.
9. Germain DP et al. Ten-year outcome of enzyme replacement therapy with agalsidase beta in patients with Fabry disease.. *Journal of medical genetics* [published online ahead of print: March 20, 2015]; doi:10.1136/jmedgenet-2014-102797
10. Mehta A et al. Enzyme replacement therapy with agalsidase alfa in patients with Fabry's disease: an analysis of registry data.. *Lancet* 2009;374(9706):1986–1996.
11. Hughes DA et al. Oral pharmacological chaperone migalastat compared with enzyme replacement therapy in Fabry disease: 18-month results from the randomised phase III ATTRACT study.. *Journal of medical genetics* 2016;jmedgenet-2016-104178.
12. Mauer M et al. Reduction of podocyte globotriaosylceramide content in adult male patients with Fabry disease with amenable GLA mutations following 6 months of migalastat treatment.. *Journal of medical genetics* 2017;54(11):781–786.
13. Thurberg BL et al. Globotriaosylceramide accumulation in the Fabry kidney is cleared from multiple cell types after enzyme replacement therapy.. *Kidney international* 2002;62(6):1933–1946.
14. Tøndel C et al. Agalsidase benefits renal histology in young patients with Fabry disease.. *Journal of the American Society of Nephrology : JASN* 2013;24(1):137–148.
15. Gödel M et al. Role of mTOR in podocyte function and diabetic nephropathy in humans and mice.. *The Journal of clinical investigation* 2011;121(6):2197–2209.
16. Rinschen MM et al. A Multi-layered Quantitative In Vivo Expression Atlas of the Podocyte Unravels Kidney Disease Candidate Genes.. *Cell reports* 2018;23(8):2495–2508.
17. Puelles VG et al. mTOR-mediated podocyte hypertrophy regulates glomerular integrity in mice and humans. *Jci Insight* 2019;4(18):e99271.
18. Kopp JB et al. Podocytopathies. *Nat Rev Dis Primers* 2020;6(1):68.
19. Wanner N et al. Unraveling the role of podocyte turnover in glomerular aging and injury.. *Journal of the American Society of Nephrology : JASN* 2014;25(4):707–716.
20. Berger K et al. The Regenerative Potential of Parietal Epithelial Cells in Adult Mice.. *Journal of the American Society of Nephrology : JASN* [published online ahead of print: January 9, 2014]; doi:10.1681/asn.2013050481

21. Najafian B et al. Progressive podocyte injury and globotriaosylceramide (GL-3) accumulation in young patients with Fabry disease. *Kidney international* 2010;79(6):663–670.
22. Tøndel C, Bostad L, Hirth A, Svarstad E. Renal biopsy findings in children and adolescents with Fabry disease and minimal albuminuria. *American journal of kidney diseases : the official journal of the National Kidney Foundation* 2008;51(5):767–776.
23. Miller JJ et al. α -Galactosidase A-deficient rats accumulate glycosphingolipids and develop cardiorenal phenotypes of Fabry disease. *FASEB journal : official publication of the Federation of American Societies for Experimental Biology* 2018;fj201800771R.
24. Ohshima T et al. alpha-Galactosidase A deficient mice: a model of Fabry disease. *Proc National Acad Sci* 1997;94(6):2540–2544.
25. Taguchi A et al. A symptomatic Fabry disease mouse model generated by inducing globotriaosylceramide synthesis. *The Biochemical journal* 2013;456(3):373–383.
26. Saleem MA et al. A conditionally immortalized human podocyte cell line demonstrating nephrin and podocin expression. [Internet]. *Journal of the American Society of Nephrology : JASN* 2002;13(3):630–638.
27. Jinek M et al. A Programmable Dual-RNA-Guided DNA Endonuclease in Adaptive Bacterial Immunity. *Science* 2012;337(6096):816–821.
28. Ran FA et al. Genome engineering using the CRISPR-Cas9 system. *Nature protocols* 2013;8(11):2281–2308.
29. Hartleben B et al. Autophagy influences glomerular disease susceptibility and maintains podocyte homeostasis in aging mice. *The Journal of clinical investigation* 2010;120(4):1084–1096.
30. Sevlever D, Jiang P, Yen S-HC. Cathepsin D Is the Main Lysosomal Enzyme Involved in the Degradation of α -Synuclein and Generation of Its Carboxy-Terminally Truncated Species. *Biochemistry-us* 2008;47(36):9678–9687.
31. McGlinchey RP, Lee JC. Cysteine cathepsins are essential in lysosomal degradation of α -synuclein. *Proc National Acad Sci* 2015;112(30):9322–9327.
32. Ferri L et al. Fabry disease: polymorphic haplotypes and a novel missense mutation in the GLA gene. *Clin Genet* 2011;81(3):224–33.
33. Miller JJ et al. Neuropathic pain in a Fabry disease rat model. *JCI insight* 2018;3(6). doi:10.1172/jci.insight.99171
34. Labilloy A et al. Altered dynamics of a lipid raft associated protein in a kidney model of Fabry disease. *Molecular Genetics and Metabolism* [published online ahead of print: October 19, 2013]; doi:10.1016/j.ymgme.2013.10.010
35. Liebau MC et al. Dysregulated Autophagy Contributes to Podocyte Damage in Fabry's Disease. *Plos One* 2013;8(5):e63506.
36. Chévrier M et al. Autophagosome maturation is impaired in Fabry disease. 2010;6(5):589–599.
37. Bourdenx M et al. Nanoparticles restore lysosomal acidification defects: Implications for Parkinson and other lysosomal-related diseases. *Autophagy* 2016;12(3):472–83.
38. Deganuto M et al. Altered intracellular redox status in Gaucher disease fibroblasts and impairment of adaptive response against oxidative stress. *J Cell Physiol* 2007;212(1):223–235.
39. Shen J-S et al. Globotriaosylceramide induces oxidative stress and up-regulates cell adhesion molecule expression in Fabry disease endothelial cells. *Mol Genet Metab* 2008;95(3):163–8.
40. Mata M de la et al. Pharmacological Chaperones and Coenzyme Q10 Treatment Improves Mutant β -Glucocerebrosidase Activity and Mitochondrial Function in Neuronopathic Forms of Gaucher Disease. *Sci Rep-uk* 2015;5(1):10903.
41. Mata M de la et al. Mitochondrial Dysfunction in Lysosomal Storage Disorders. *Dis Basel Switz* 2016;4(4):31.
42. Brinkkoetter PT et al. Anaerobic Glycolysis Maintains the Glomerular Filtration Barrier Independent of Mitochondrial Metabolism and Dynamics. *Cell reports* 2019;27(5):1551-1566.e5.
43. Dasgupta N et al. Gaucher disease: transcriptome analyses using microarray or mRNA sequencing in a Gba1 mutant mouse model treated with velaglucerase alfa or imiglucerase. *Plos One* 2013;8(10):e74912.
44. Shin Y-J et al. Substrate-specific gene expression profiles in different kidney cell types are associated with Fabry disease. *Mol Med Rep* 2015;12(4):5049–57.
45. Slaats GG et al. Urine-derived cells: a promising diagnostic tool in Fabry disease patients. *Sci Rep-uk* 2018;8(1):11042.
46. Jehn U et al. α -Galactosidase a Deficiency in Fabry Disease Leads to Extensive Dysregulated Cellular Signaling Pathways in Human Podocytes. *Int J Mol Sci* 2021;22(21):11339.

47. Gonzalez A, Valeiras M, Sidransky E, Tayebi N. Lysosomal integral membrane protein-2: a new player in lysosome-related pathology.. *Mol Genet Metab* 2013;111(2):84-91.
48. Vogiatzi T, Xilouri M, Vekrellis K, Stefanis L. Wild type alpha-synuclein is degraded by chaperone-mediated autophagy and macroautophagy in neuronal cells.. *J Biological Chem* 2008;283(35):23542-56.
49. Huarcaya SP et al. Recombinant pro-CTSD (cathepsin D) enhances SNCA/ α -Synuclein degradation in α -Synucleinopathy models. *Autophagy* [published online ahead of print: 2022]; doi:10.1080/15548627.2022.2045534
50. Magalhaes J et al. Autophagic lysosome reformation dysfunction in glucocerebrosidase deficient cells: relevance to Parkinson disease. *Human molecular genetics* 2016;25(16):3432-3445.
51. Picillo M et al. Parkinsonism due to A53E α -synuclein gene mutation: Clinical, genetic, epigenetic, and biochemical features. *Movement Disord* 2018;33(12):1950-1955.
52. Rosborough K, Patel N, Kalia LV. α -Synuclein and Parkinsonism: Updates and Future Perspectives. *Curr Neurol Neurosci* 2017;17(4):31.
53. Morris KV, Chan SW-L, Jacobsen SE, Looney DJ. Small interfering RNA-induced transcriptional gene silencing in human cells.. *Science (New York, N.Y.)* 2004;305(5688):1289-1292.
54. Martinez-Vicente M et al. Dopamine-modified alpha-synuclein blocks chaperone-mediated autophagy.. *The Journal of clinical investigation* 2008;118(2):777-788.
55. Tenreiro S et al. Phosphorylation Modulates Clearance of Alpha-Synuclein Inclusions in a Yeast Model of Parkinson's Disease. *PLoS genetics* 2014;10(5):e1004302-23.
56. Dehay B et al. Targeting α -synuclein for treatment of Parkinson's disease: mechanistic and therapeutic considerations. *Lancet Neurology* 2015;14(8):855-866.
57. Gitler AD et al. The Parkinson's disease protein α -synuclein disrupts cellular Rab homeostasis. *Proc National Acad Sci* 2007;105(1):145-150.
58. Martin LJ et al. Parkinson's Disease α -Synuclein Transgenic Mice Develop Neuronal Mitochondrial Degeneration and Cell Death. *J Neurosci* 2006;26(1):41-50.
59. Adams J et al. Autophagy-lysosome pathway alterations and alpha-synuclein up-regulation in the subtype of neuronal ceroid lipofuscinosis, CLN5 disease.. *Sci Rep-uk* 2019;9(1):151.
60. Wise AH et al. Parkinson's disease prevalence in Fabry disease: A survey study.. *Molecular genetics and metabolism reports* 2018;14:27-30.
61. Najafian B et al. Accumulation of Globotriaosylceramide in Podocytes in Fabry Nephropathy Is Associated with Progressive Podocyte Loss.. *J Am Soc Nephrol Jasn* 2020;ASN.2019050497.
62. Najafian B et al. One Year of Enzyme Replacement Therapy Reduces Globotriaosylceramide Inclusions in Podocytes in Male Adult Patients with Fabry Disease.. *PLoS one* 2016;11(4):e0152812.
63. Braun F et al. Enzyme Replacement Therapy Clears Gb3 Deposits from a Podocyte Cell Culture Model of Fabry Disease but Fails to Restore Altered Cellular Signaling. *Cell Physiol Biochem* 2019;52(5):1139-1150.
64. Veen SJ van der et al. Early start of enzyme replacement therapy in pediatric male patients with classical Fabry disease is associated with attenuated disease progression. *Mol Genet Metab* 2022;135(2):163-169.
65. Hopkin RJ et al. Clinical outcomes among young patients with Fabry disease who initiated agalsidase beta treatment before 30 years of age: An analysis from the Fabry registry. *Mol Genet Metab* 2022;106967.
66. Rosenbluth JM, Mays DJ, Pino MF, Tang LJ, Pietenpol JA. A gene signature-based approach identifies mTOR as a regulator of p73.. *Mol Cell Biol* 2008;28(19):5951-64.
67. Subramanian A et al. A Next Generation Connectivity Map: L1000 Platform and the First 1,000,000 Profiles. *Cell* 2017;171(6):1437-1452.e17.
68. Mittal S et al. β 2-Adrenoreceptor is a regulator of the α -synuclein gene driving risk of Parkinson's disease. *Science* 2017;357(6354):891-898.
69. Huber TB et al. Catecholamines modulate podocyte function.. *J Am Soc Nephrol* 1998;9(3):335-345.
70. Lee J-H et al. β 2-adrenergic Agonists Rescue Lysosome Acidification and Function in PSEN1 Deficiency by Reversing Defective ER-to-lysosome Delivery of CIC-7. *J Mol Biol* 2020;432(8):2633-2650.
71. Maor G, Rapaport D, Horowitz M. The effect of mutant GBA1 on accumulation and aggregation of α -synuclein. *Hum Mol Genet* 2019;28(11):1768-1781.
72. Li H et al. Mitochondrial dysfunction and mitophagy defect triggered by heterozygous GBA mutations. *Autophagy* 2018;15(1):113-130.
73. Sardi SP et al. Glucosylceramide synthase inhibition alleviates aberrations in synucleinopathy models.. *P Natl Acad Sci Usa* 2017;114(10):2699-2704.
74. Tayebi N et al. Glucocerebrosidase haploinsufficiency in A53T α -synuclein mice impacts disease onset and course.. *Mol Genet Metab* 2017;122(4):198-208.

75. Gago MF et al. Parkinson's Disease and Fabry Disease: Clinical, Biochemical and Neuroimaging Analysis of Three Pedigrees.. *J Park Dis* 2019;1–12.
76. Nelson MP et al. Autophagy-lysosome pathway associated neuropathology and axonal degeneration in the brains of alpha-galactosidase A-deficient mice. *Acta Neuropathologica Commun* 2014;2(1):20.
77. Hale LJ et al. 3D organoid-derived human glomeruli for personalised podocyte disease modelling and drug screening.. *Nature communications* 2018;9(1):5167.
78. Germain DP et al. The effect of enzyme replacement therapy on clinical outcomes in female patients with Fabry disease - A systematic literature review by a European panel of experts.. *Molecular Genetics and Metabolism* [published online ahead of print: September 27, 2018]; doi:10.1016/j.ymgme.2018.09.007
79. Toyoda M, Najafian B, Kim Y, Caramori ML, Mauer M. Podocyte Detachment and Reduced Glomerular Capillary Endothelial Fenestration in Human Type 1 Diabetic Nephropathy. *Diabetes* 2007;56(8):2155–2160.
80. Zhou T et al. Generation of human induced pluripotent stem cells from urine samples.. *Nature protocols* 2012;7(12):2080–2089.
81. Yasuda-Yamahara M et al. FERMT2 links cortical actin structures, plasma membrane tension and focal adhesion function to stabilize podocyte morphology.. *Matrix biology : journal of the International Society for Matrix Biology* 2018;68–69:263–279.
82. Grahammer F et al. A flexible, multilayered protein scaffold maintains the slit in between glomerular podocytes. *Jci Insight* 2016;1(9):e86177.
83. Schell C et al. The FERM protein EPB41L5 regulates actomyosin contractility and focal adhesion formation to maintain the kidney filtration barrier. *Proc National Acad Sci* 2017;114(23):E4621–E4630.
84. Cheng F et al. Network-based approach to prediction and population-based validation of in silico drug repurposing. *Nat Commun* 2018;9(1):2691.
85. Ghiassian SD, Menche J, Barabási A-L. A DIseAse MOdule Detection (DIAMONd) algorithm derived from a systematic analysis of connectivity patterns of disease proteins in the human interactome.. *Plos Comput Biol* 2015;11(4):e1004120.
86. Halu A et al. Exploring the cross-phenotype network region of disease modules reveals concordant and discordant pathways between chronic obstructive pulmonary disease and idiopathic pulmonary fibrosis.. *Hum Mol Genet* 2019;28(14):2352–2364.
87. Beutler E, Kuhl W. Purification and properties of human alpha-galactosidases.. *J Biological Chem* 1972;247(22):7195–200.
88. Kint JA. Fabry's Disease: Alpha-Galactosidase Deficiency. *Science* 1970;167(3922):1268–1269.
89. Mayes JS, Scheerer JB, Sifers RN, Donaldson ML. Differential assay for lysosomal alpha-galactosidases in human tissues and its application to Fabry's disease. *Clin Chim Acta* 1981;112(2):247–251.
90. Shen J-S et al. Mannose receptor-mediated delivery of moss-made α -galactosidase A efficiently corrects enzyme deficiency in Fabry mice.. *J Inherit Metab Dis* 2015;39(2):293–303.
91. Luciani A et al. Impaired Lysosomal Function Underlies Monoclonal Light Chain-Associated Renal Fanconi Syndrome.. *J Am Soc Nephrol Jasn* 2015;27(7):2049–61.
92. Kubota C et al. Constitutive reactive oxygen species generation from autophagosome/lysosome in neuronal oxidative toxicity.. *J Biological Chem* 2009;285(1):667–74.
93. Bligh EG, Dyer WJ. A RAPID METHOD OF TOTAL LIPID EXTRACTION AND PURIFICATION. *Can J Biochem Phys* 1959;37(8):911–917.
94. Takahashi M et al. Normalization of Overexpressed α -Synuclein Causing Parkinson's Disease By a Moderate Gene Silencing With RNA Interference.. *Mol Ther Nucleic Acids* 2015;4(Lancet 373 2009):e241.
95. Rogg M et al. The WD40-domain containing protein CORO2B is specifically enriched in glomerular podocytes and regulates the ventral actin cytoskeleton.. *Scientific Reports* 2017;7(1):15910.
96. Skrunes R et al. Long-Term Dose-Dependent Agalsidase Effects on Kidney Histology in Fabry Disease.. *Clinical journal of the American Society of Nephrology : CJASN* 2017;12(9):1470–1479.
97. Ruifrok AC, Johnston DA. Quantification of histochemical staining by color deconvolution.. *Anal Quantitative Cytol Histology Int Acad Cytol Am Soc Cytol* 2001;23(4):291–9.
98. Khanna R et al. The Pharmacological Chaperone 1-Deoxygalactonojirimycin Reduces Tissue Globotriaosylceramide Levels in a Mouse Model of Fabry Disease. *Mol Ther* 2010;18(1):23–33.

Figure Legends

Figure 1: (A) Transmission electron microscopy (TEM) comparison of foot processes between control vs Fabry kidney biopsy before and after ERT with many foot processes widened in both untreated and after ERT Fabry biopsies. Asterisks show Gb3 inclusions in podocytes. (B) Significant decrease of podocyte Gb3 inclusions after ERT but persistence of increased foot process width. (C) Schematic overview of *GLA* knock-out (KO) podocyte generation by CRISPR/Cas9 genome editing. (D) Western blots show a complete absence of *GLA* expression in several *GLA*-KO clones. (E) Abolished *GLA* activity in two KO clones compared to WT cells. (F) Mass spectrometry analysis confirms the accumulation of GB3-C24-0 isoform in KO cells, normalized upon 96 hours of alpha-GAL therapy (n=3). (G) TEM shows zebra bodies exclusively in *GLA*-KO clones (red arrows). While WT cells depict a normal ultrastructure, aGAL-treated KO cells have remnant vacuoles (green arrows) without zebra bodies. Scalebar represents 1µm. (H) Lysosomal visualization using LAMP1 staining in differentiated WT and KO cells reveals an increased number and size (arrows) of lysosomes in the *GLA*-KO cells. Scalebars represent 10µm. (I) Quantification of lysosomal area (n=14), pH (n=12) and ROS production (n=8). (J) Seahorse XFp experiments confirms a normal mitochondrial function in KO cells (N=8). (K) Mitochondrial import receptor subunit (TOM20) staining in WT and KO cells is equally abundant and normally distributed. TEM images confirm a normal mitochondrial ultrastructure in KO cells. Scalebars indicating 10µm in IF and 500nm in EM.

Violin plots indicating median (red) and upper and lower quartile (blue), **P<0.01, ***P<0.001, ****P<0.0001.

Statistical tests used – 1-Way-ANOVA (multiple comparison test - Tukey)

Figure 2: (A) Schematic overview of mass spectrometry analysis using SILAC labelled WT and KO clones. Mass spectrometry yielded 2248 proteins among which 321 proteins are lysosomal enriched. (B) The top ten up and down regulated lysosomal enriched proteins. (C) Network based analysis of up- and downregulated lysosomal proteins associated to *GLA* knock-out (KO). Nodes represent genes and are connected if there is a known protein interaction between them. The node size is proportional to the number of its connections. Red and blue nodes represent up- and downregulated seed proteins, respectively. Light-red and light-blue nodes represent the respective DIAMOND proteins. *GLA* is depicted as green node. Pink nodes indicate shared proteins between the two modules. The separate network and Venn diagram on the right shows the number and interaction partners of SNCA.

Figure 3: (A) Mean cathepsin D activity in WT cells and two KO clones showing no differences in enzyme activity (n=3). (B) Western blots of SNCA and TUBA in vehicle and aGAL treated WT and KO cells with quantification confirming the over-expression and resistance of SNCA protein to aGAL treatment (n=4). (C) Human SNCA ELISA depicting SNCA accumulation in KO clones and resistance to substrate reduction therapy using venglustat (n=5) (D) SNCA staining in representative images and quantification of human renal biopsies showing increase in untreated Fabry samples with resistant accumulation in patients who underwent 5 years of ERT (n=5). Scalebars indicating 50µm. ****P<0,0001

Statistical tests used – A, B, C & D: 1-Way-ANOVA (multiple comparison test - Tukey)

Figure 4: (A) Representative western blot confirming the efficacy of siRNA targeting SNCA in WT and knock-out (KO) clones (n=4). (B) Quantification of lysosomal area, pH and ROS production upon SNCA siRNA treatment (n=18). (C) A representative western blot confirming the overexpression of SNCA in WT cells (n=4). (D) LAMP-1 immunofluorescence staining shows an increase in lysosomal aggregation upon SNCA overexpression (arrow). Scalebars represent 10 μ m. (E) Quantification of lysosomal area (n=20), pH (n=8) and ROS production (n=12) upon SNCA overexpression. Violin plots indicate median (red) and upper and lower quartile (blue). *P<0.05, **P<0.01, ***P<0.001, ****P <0.0001
Statistical tests used – B: 1-Way-ANOVA (multiple comparison test - Tukey); E: t-Test

Figure 5: (A) Connectivity mapping showing anti-Fabry compounds with the β 2-adrenergic receptor agonist Orciprenaline exhibiting the highest score. (B) Western blots show the expression of SNCA in WT, untreated GLA-KO and KO cells treated with 20 μ M Clenbuterol and 10 μ M Orciprenaline (n=6). (C) Western blots depict the expression of Lamp-1 and ACTN4 in WT, untreated GLA-KO and KO cells treated with aGAL, 20 μ M Clenbuterol, and combined therapy (n=6). (D) Lysosomal pH analysis in all conditions demonstrates independent and additive effects of β 2-adrenergic receptor agonist in GLA-KO cells (n=6). (E) Lysosomal ROS analysis demonstrates independent and additive effects of β 2-adrenergic receptor agonist in GLA-KO cells (n=6). (F) Schematic summary depicting the overall findings of the manuscript: Fabry podocyte lysosomes are characterized by increased size, pH and ROS production with subsequently decreased function due to Gb3 and SNCA accumulation. This phenotype can be ameliorated through enzyme replacement therapy combined with compounds decreasing SNCA accumulation like beta-receptor agonists. Bar graphs depict standard deviation. *P<0.05, **P<0.01, ***P<0.001, ****P <0.0001
Statistical tests used – 1-Way-ANOVA (multiple comparison test - Tukey)

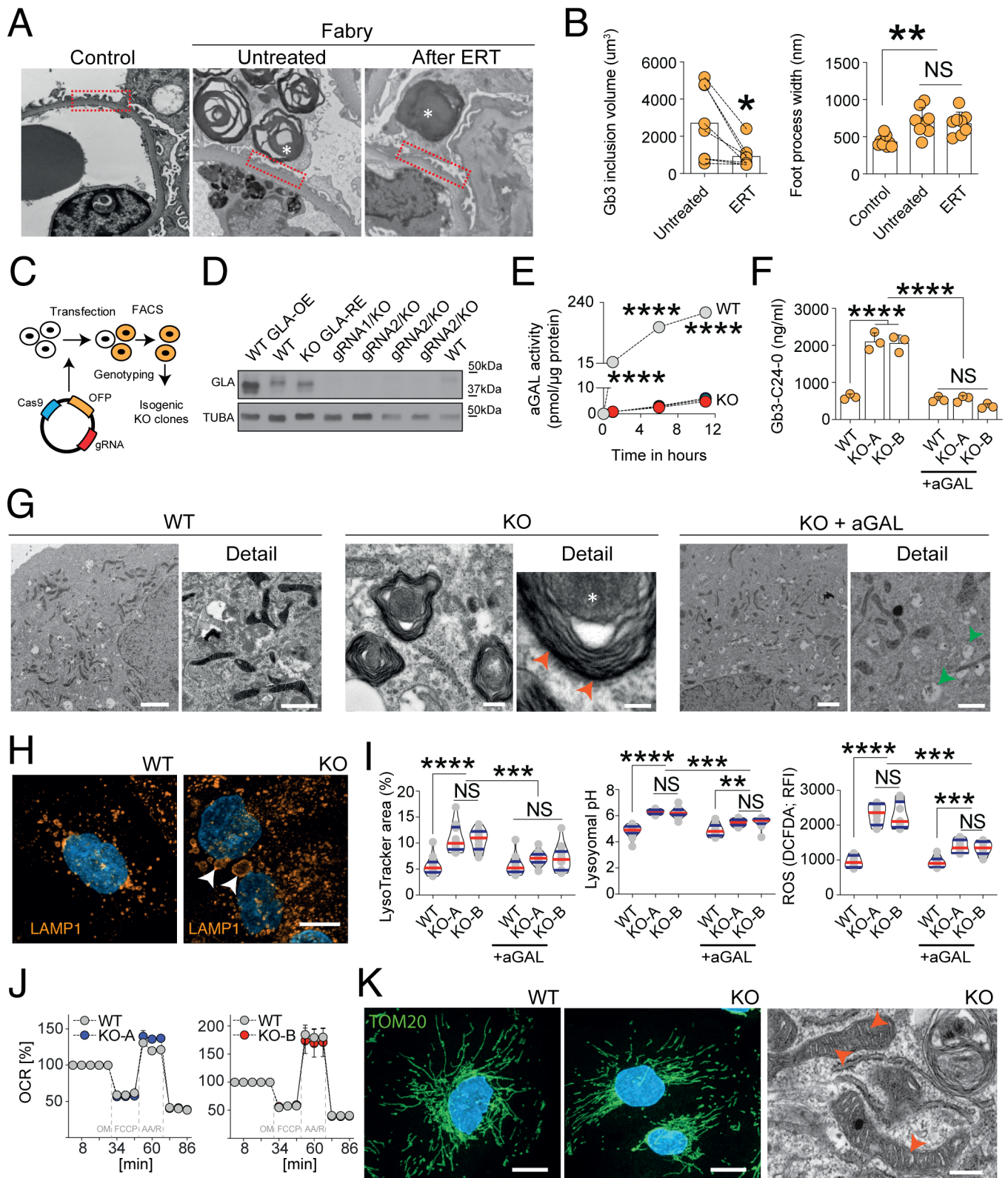
Fig. 1

Figure 1: (A) Transmission electron microscopy (TEM) comparison of foot processes between control vs Fabry kidney biopsy before and after ERT with many foot processes widened in both untreated and after ERT Fabry biopsies. Asterisks show Gb3 inclusions in podocytes. (B) Significant decrease of podocyte Gb3 inclusions after ERT but persistence of increased foot process width. (C) Schematic overview of GLA knock-out (KO) podocyte generation by CRISPR/Cas9 genome editing. (D) Western blots show a complete absence of GLA expression in several GLA-KO clones. (E) Abolished GLA activity in two KO clones compared to WT cells. (F) Mass spectrometry analysis confirms the accumulation of GB3-C24-0 isoform in KO cells, normalized upon 96 hours of alpha-GAL therapy (n=3). (G) TEM shows zebra bodies exclusively in GLA-KO clones (red arrows). While WT cells depict a normal ultrastructure, aGAL-treated KO cells have remnant vacuoles (green arrows) without zebra bodies. Scalebar represents 1 μm . (H) Lysosomal visualization using LAMP1 staining in differentiated WT and KO cells reveals an increased number and size (arrows) of lysosomes in the GLA-KO cells. Scalebars represent 10 μm . (I) Quantification of lysosomal area (n=14), pH (n=12) and ROS production (n=8). (J) Seahorse XFp experiments confirm a normal mitochondrial function in KO cells (N=8). (K) Mitochondrial import receptor subunit (TOM20) staining in WT and KO cells is equally abundant and normally distributed. TEM images confirm a normal mitochondrial ultrastructure in KO cells. Scalebars indicating 10 μm in IF and 500nm in EM. Violin plots indicating median (red) and upper and lower quartile (blue), **P<0.01, ***P<0.001, ****P<0.0001. Statistical tests used – 1-Way-ANOVA (multiple comparison test – Tukey)

Fig. 2

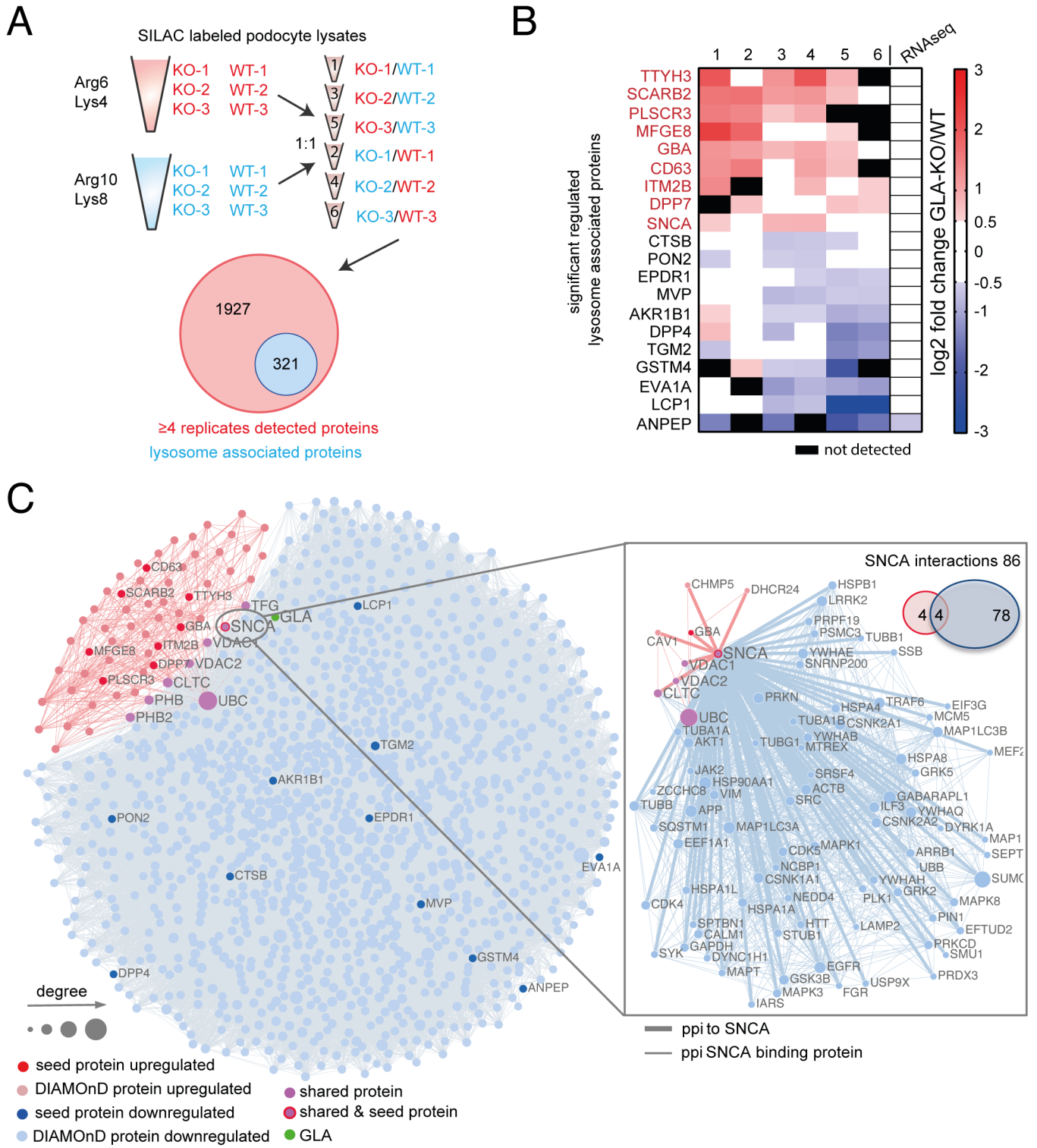


Figure 2: (A) Schematic overview of mass spectrometry analysis using SILAC labelled WT and KO clones. Mass spectrometry yielded 2248 proteins among which 321 proteins are lysosomal enriched. (B) The top ten up and down regulated lysosomal enriched proteins. (C) Network based analysis of up- and downregulated lysosomal proteins associated to GLA knock-out (KO). Nodes represent genes and are connected if there is a known protein interaction between them. The node size is proportional to the number of its connections. Red and blue nodes represent up- and downregulated seed proteins, respectively. Light-red and light-blue nodes represent the respective DIAMOND proteins. GLA is depicted as green node. Pink nodes indicate shared proteins between the two modules. The separate network and Venn diagram on the right shows the number and interaction partners of SNCA.

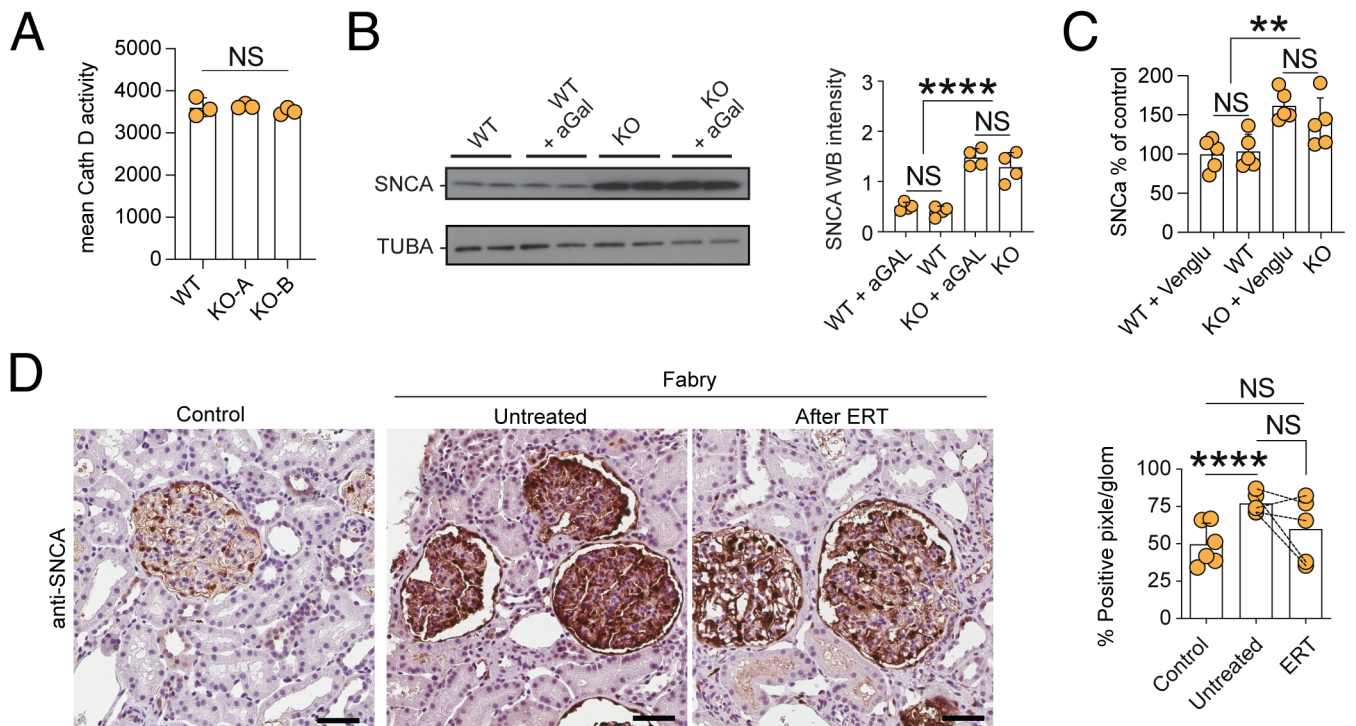
Fig. 3

Figure 3: (A) Mean cathepsin D activity in WT cells and two KO clones showing no differences in enzyme activity (n=3). (B) Western blots of SNCA and TUBA in vehicle and aGAL treated WT and KO cells with quantification confirming the over-expression and resistance of SNCA protein to aGAL treatment (n=4). (C) Human SNCA ELISA depicting SNCA accumulation in KO clones and resistance to substrate reduction therapy using venglustat (n=5) (D) SNCA staining in representative images and quantification of human renal biopsies showing increase in untreated Fabry samples with resistant accumulation in patients who underwent 5 years of ERT (n=5). Scalebars indicating 50 μ m. ****P<0,0001

Statistical tests used – A, B, C & D: 1-Way-ANOVA (multiple comparison test - Tukey)

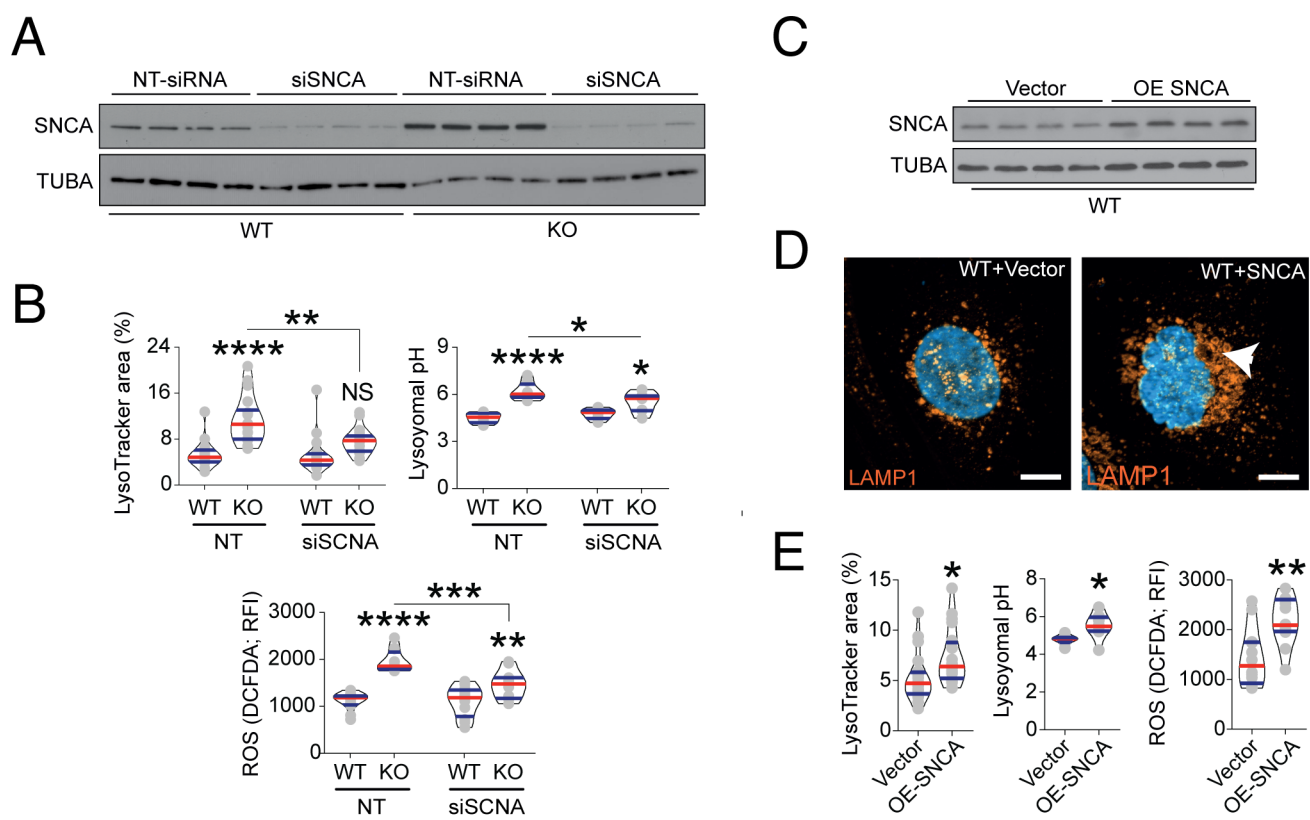
Fig. 4

Figure 4: (A) Representative western blot confirming the efficacy of siRNA targeting SNCA in WT and knock-out (KO) clones (n=4). (B) Quantification of lysosomal area, pH and ROS production upon SNCA siRNA treatment (n=18). (C) A representative western blot confirming the overexpression of SNCA in WT cells (n=4). (D) LAMP-1 immunofluorescence staining shows an increase in lysosomal aggregation upon SNCA overexpression (arrow). Scalebars represent 10µm. (E) Quantification of lysosomal area (n=20), pH (n=8) and ROS production (n=12) upon SNCA overexpression. Violin plots indicate median (red) and upper and lower quartile (blue). *P<0.05, **P<0.01, ***P<0.001, ****P <0.0001

Statistical tests used – B: 1-Way-ANOVA (multiple comparison test - Tukey); E: t-Test

Fig. 5

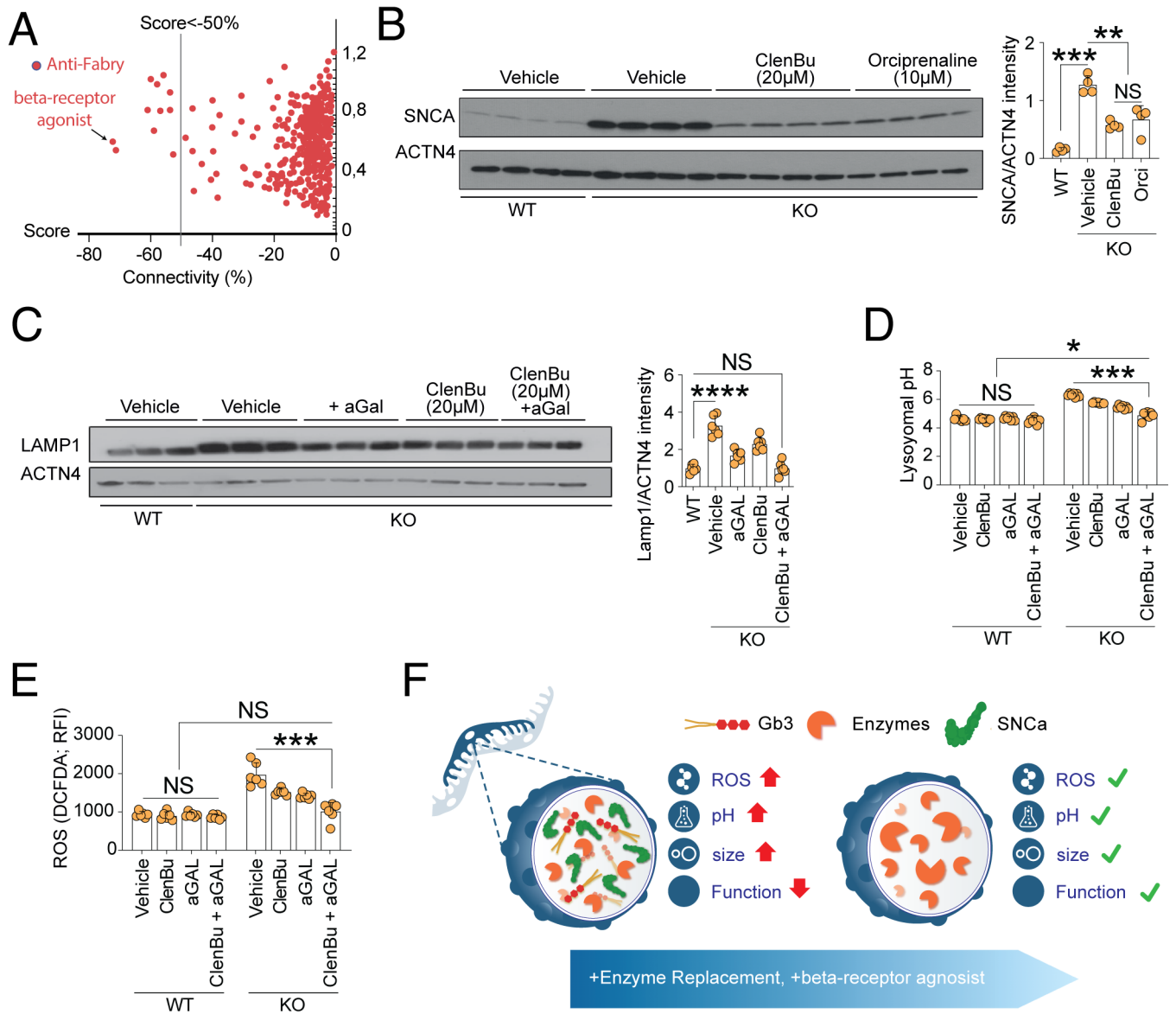


Figure 5: (A) Connectivity mapping showing anti-Fabry compounds with the β -adrenergic receptor agonist Orciprenaline exhibiting the highest score. (B) Western blots show the expression of SNCA in WT, untreated GLA-KO and KO cells treated with 20 μ M Clenbuterol and 10 μ M Orciprenaline (n=6). (C) Western blots depict the expression of Lamp-1 and ACTN4 in WT, untreated GLA-KO and KO cells treated with aGal, 20 μ M Clenbuterol, and combined therapy (n=6). (D) Lysosomal pH analysis in all conditions demonstrates independent and additive effects of β -adrenergic receptor agonist in GLA-KO cells (n=6). (E) Lysosomal ROS analysis demonstrates independent and additive effects of β -adrenergic receptor agonist in GLA-KO cells (n=6). (F) Schematic summary depicting the overall findings of the manuscript: Fabry podocyte lysosomes are characterized by increased size, pH and ROS production with subsequently decreased function due to Gb3 and SNCA accumulation. This phenotype can be ameliorated through enzyme replacement therapy combined with compounds decreasing SNCA accumulation like beta-receptor agonists. Bar graphs depict standard deviation. *P<0.05, **P<0.01, ***P<0.001, ****P<0.0001. Statistical tests used – 1-Way-ANOVA (multiple comparison test - Tukey)